

Auto-correlation Function Study of Scattered Light Intensity

Yong Sun*

October 9, 2018

Abstract

In this work, the particle size distribution measured using the dynamic light scattering (DLS) technique is compared with that obtained from the static light scattering (SLS) technique or provided by the supplier measured using the Transmission Electron Microscopy (TEM) technique for dilute Poly(*N*-isopropylacrylamide) microgel and standard polystyrene latex samples in dispersion respectively. The results show that the narrow particle size distribution that can be measured accurately using the SLS technique is not suited to the determination by the DLS technique and the particle size distribution obtained from the DLS technique is different from the value provided by the supplier. With the assistance of the simulated data of the normalized time auto-correlation function of the scattered light intensity $g^{(2)}(\tau)$, the effects of the particle size distribution on the nonexponentiality of $g^{(2)}(\tau)$ measured at a scattering angle of 30° are investigated. The analysis reveals that the influences of the particle size distribution are small on the nonexponentiality of $g^{(2)}(\tau)$ and very large on the initial slope of the logarithm of $g^{(2)}(\tau)$. The values of the apparent hydrodynamic radius are also largely influenced by the particle size distribution and the difference between the distributions of the apparent hydrodynamic radius and hydrodynamic radius of particles is determined by the method of cumulants.

1 INTRODUCTION

For colloidal dispersion systems, light scattering is a widely used technique to measure the sizes of particles. One of the main applications of the dynamic light scattering (DLS) technique is to measure the sizes of spherical particles in liquid suspension. The standard method of cumulants [1–4] has been used to measure the hydrodynamic radius, or more strictly apparent hydrodynamic radius $R_{h,app}$ [5] of particles from the normalized time auto-correlation function of the scattered light intensity $g^{(2)}(\tau)$ with the assistance of the Einstein-Stokes relation, where τ is the delay time. However this method is insensitive to a

*Email: ysun2002h@yahoo.com.cn

small poly-dispersity and not suited to the accurate determination for the poly-dispersities (standard deviation/mean size) less than about 10%. For large particles, DLS technique, where it loses the accuracy of size measurements, is endeavored to use at different scattering angles in order to obtain the effective diffusion coefficient [6] or the apparent hydrodynamic radius [5] to detect small poly-dispersities.

In the previous work [7,8], I have discussed that a new radius, static radius, can be obtained from the static light scattering (SLS) technique, the particle size distribution less than 10% can be measured accurately and the three different particle sizes, static, hydrodynamic and apparent hydrodynamic radii, can be obtained using the light scattering technique. In this work, the particle size distribution measured using the DLS technique is compared with that obtained from the SLS technique or provided by the supplier measured using the Transmission Electron Microscopy (TEM) technique for dilute Poly(*N*-isopropylacrylamide) (PNIPAM) microgel and standard polystyrene latex samples in dispersion respectively. The results show that the narrow particle size distribution that can be measured accurately using the SLS technique is not suited to the determination by the DLS techniques and the particle size distribution obtained using the DLS technique is different from the value provided by the supplier. Since the method of cumulants measures the particle size distribution from the deviation between the exponentiality and $g^{(2)}(\tau)$ measured at a single scattering angle, the simulated data were thus used to explore the effects of the particle size distribution on the difference between them at a scattering angle of 30°. The analysis reveals that the effects of the particle size distribution are small on the nonexponentiality of $g^{(2)}(\tau)$ and very large on the initial slope of the logarithm of $g^{(2)}(\tau)$. The values of the apparent hydrodynamic radius are also largely influenced by the particle size distribution and the difference between the distributions of the apparent hydrodynamic radius and hydrodynamic radius of particles is determined by the method of cumulants.

2 THEORY

For dilute poly-disperse homogeneous spherical particles in dispersion where the Rayleigh-Gans-Debye (RGD) approximation is valid, the normalized time auto-correlation function of the electric field of the scattered light $g^{(1)}(\tau)$ is given by

$$g^{(1)}(\tau) = \frac{\int_0^\infty R_s^6 P(q, R_s) G(R_s) \exp(-q^2 D \tau) dR_s}{\int_0^\infty R_s^6 P(q, R_s) G(R_s) dR_s}, \quad (1)$$

where R_s is the static radius, D is the diffusion coefficient, $q = \frac{4\pi}{\lambda} n_s \sin \frac{\theta}{2}$ is the scattering vector, λ is the wavelength of the incident light in vacuo, n_s is the solvent refractive index, θ is the scattering angle, $G(R_s)$ is the number

distribution of particle sizes and the form factor $P(q, R_s)$ is

$$P(q, R_s) = \frac{9}{q^6 R_s^6} (\sin(qR_s) - qR_s \cos(qR_s))^2. \quad (2)$$

From the Einstein-Stokes relation

$$D = \frac{k_B T}{6\pi\eta_0 R_h}, \quad (3)$$

where η_0 , k_B and T are the viscosity of the solvent, Boltzmann's constant and absolute temperature respectively, the hydrodynamic radius R_h can be obtained.

Traditionally the cumulants is a standard method to measure the particle size distribution from the DLS data $g^{(2)}(\tau)$. In this work, the following equation was used to analyze the DLS data to the second moment

$$g^{(2)}(\tau) = 1 + \beta \exp(-2\langle\Gamma\rangle\tau) (1 + \mu_2\tau^2), \quad (4)$$

where $\langle\Gamma\rangle = q^2 D_e(q)$ is the average decay rate, $D_e(q)$ is the effective diffusion coefficient, μ_2 is the second moment and β is a constant that depends on the experimental geometry for a given experimental measurement. The apparent hydrodynamic radius $R_{h,app}$ can be obtained from $D_e(q)$

$$R_{h,app} = \frac{k_B T}{6\pi\eta_0 D_e}. \quad (5)$$

The relative width of the apparent hydrodynamic radius distribution is [9]

$$\frac{Width}{R_{h,app}} = \frac{\sqrt{\mu_2}}{\langle\Gamma\rangle}. \quad (6)$$

If the first cumulant is used, the value of the apparent hydrodynamic radius $R_{h,app}$ at a given scattering angle and a given delay time τ can be calculated directly using the static particle size information and the relationship between the static and hydrodynamic radii. If the DLS data during the delay time range τ_1 and τ_2 are chosen to obtain $R_{h,app}$ at a given scattering angle, the average value of apparent hydrodynamic radius can be calculated using the following equation

$$R_{h,app} \left(e^{-\frac{q^2 k_B T \tau_1}{6\pi\eta_0 R_{h,app}}} - e^{-\frac{q^2 k_B T \tau_2}{6\pi\eta_0 R_{h,app}}} \right) = \frac{\int_0^\infty R_h R_s^6 P(q, R_s) G(R_s) \left(e^{-\frac{q^2 k_B T \tau_1}{6\pi\eta_0 R_h}} - e^{-\frac{q^2 k_B T \tau_2}{6\pi\eta_0 R_h}} \right) dR_s}{\int_0^\infty R_s^6 P(q, R_s) G(R_s) R_s dR_s}. \quad (7)$$

3 EXPERIMENT

The SLS and DLS data were measured using the instrument built by ALV-Laser Vertriebsgesellschaft m.b.H (Langen, Germany). It utilizes an ALV-5000

Multiple Tau Digital Correlator and a JDS Uniphase 1145P He-Ne laser to provide a 23 mW vertically polarized laser at wavelength of 632.8 nm.

In this work, two kinds of samples were used. One is PNIPAM submicron spheres and the other is standard polystyrene latex spheres. The samples used in this work have been detailed before [7]. The four PNIPAM microgel samples PNIPAM-0, PNIPAM-1, PNIPAM-2 and PNIPAM-5 were named according to the molar ratios n_B/n_N of cross-linker N, N' -methylenebisacrylamide over N -isopropylacrylamide. The sulfate polystyrene latex with a normalized mean radius of 33.5 nm and surfactant-free sulfate polystyrene latex of 55 nm were named Latex-1 and Latex-2 respectively.

4 DATA ANALYSIS

In this section, the particle size information obtained using the method of cumulants from the DLS data is compared with the commercial values for the standard polystyrene latex samples and the values obtained using the SLS technique for the PNIPAM submicron spheres.

4.1 Standard polystyrene latex samples

When Eq. 4 was used to fit the data of Latex-1 measured at a temperature of 298.45 K and a scattering angle of 30° under the conditions of $\mu_2 = 0$ and $\mu_2 \neq 0$ respectively, it was found that the results of $\langle \Gamma \rangle$ and μ_2 depend on the delay time range being fit, as shown in Table 1. If a small delay time range is chosen, the parameters are not well-determined. As the delay time range is increased, the uncertainties in parameters decrease and $\langle \Gamma \rangle$ and μ_2 stabilize. From Eq. 6, the relative width of the apparent hydrodynamic radius distribution is about 0.26.

Delay time (s)	$\langle \Gamma \rangle_{first} (s^{-1})$	χ^2	$\langle \Gamma \rangle_{two} (s^{-1})$	$\mu_2 (s^{-2})$	χ^2
2×10^{-7} to 0.00102	315.6 ± 1.2	0.34	323.1 ± 3.4	21000 ± 7000	0.27
2×10^{-7} to 0.00154	313.5 ± 0.9	0.40	321.1 ± 2.4	15000 ± 4000	0.26
2×10^{-7} to 0.00364	311.1 ± 0.7	0.60	319.7 ± 1.8	12000 ± 2000	0.26
2×10^{-7} to 0.00364	310.0 ± 0.6	0.73	318.3 ± 1.4	9000 ± 1000	0.27
2×10^{-7} to 0.00568	309.4 ± 0.6	0.81	317.1 ± 1.2	8000 ± 1000	0.28
2×10^{-7} to 0.00896	309.3 ± 0.6	0.80	316.6 ± 1.2	7000 ± 1000	0.29
2×10^{-7} to 0.01306	309.3 ± 0.6	0.82	316.8 ± 1.2	7000 ± 1000	0.31

Table 1: The fit results obtained using Eq. 4 with $\mu_2 = 0$ and $\mu_2 \neq 0$ respectively for Latex-1 at different delay time ranges, a scattering angle of 30° and a temperature of 298.45 K.

Fit values obtained using both procedures are listed in Table 2 for five independent DLS data measured at a scattering angle of 30° and during the delay

time range from 2×10^{-7} to 0.00896 s. The fit results show that the average values of decay rate are consistent and the values of μ_2 have some difference. The relative width of the apparent hydrodynamic radius is from 0.23 to 0.28. However, from the particle size information provided by the supplier, the relative width of the radius distribution is only 0.07. The width of distribution obtained using the DLS technique at a scattering angle of 30° is much larger than that obtained using TEM technique. The value of the apparent hydrodynamic radius is 37.29 ± 0.08 nm using the first cumulant method and 36.5 ± 0.2 nm using the first two cumulant method. The value of the apparent hydrodynamic radius obtained from the DLS technique for Latex-1 at a scattering angle of 30° is not equal to the mean radius 33.5 nm provided by the supplier.

	$\langle \Gamma \rangle_{first} (s^{-1})$	χ^2	$\langle \Gamma \rangle_{two} (s^{-1})$	$\mu_2 (s^{-2})$	χ^2
1	308.4 ± 0.6	0.69	$314. \pm 1.$	5000 ± 1000	0.42
2	310.1 ± 0.6	0.75	$318. \pm 1.$	7000 ± 1000	0.18
3	309.3 ± 0.6	0.80	$317. \pm 1.$	7000 ± 1000	0.29
4	308.8 ± 0.6	0.88	$317. \pm 1.$	8000 ± 1000	0.25
5	309.9 ± 0.6	0.64	$316. \pm 1.$	6000 ± 1000	0.27

Table 2: The fit results obtained using Eq. 4 with $\mu_2 = 0$ and $\mu_2 \neq 0$ respectively for the five independent DLS data of Latex-1 measured at a scattering angle of 30° and a temperature of 298.45 K.

The intensity-intensity correlation function $g^{(2)}(\tau)$ measured at a scattering angle 30° is shown in Fig. 1. Figure 1a shows the data of $g^{(2)}(\tau)$ and a fit of Eq. 4 to the data with $\mu_2 = 0$ during the delay time range from 2×10^{-7} to 0.00896 s. The residuals $(y_i - y_{fit})/\sigma_i$ show systematic variations with the delay time, where y_i , y_{fit} and σ_i are the data, the fit value and the uncertainty in the data at a given delay time τ_i , respectively. Figure 1b shows the same data with a fit of Eq. 4 in which $\mu_2 \neq 0$. The residuals show systematic variations again.

When Eq. 4 was used to fit the DLS data of Latex-1 measured at a scattering angle of 90° and the same temperature for $\mu_2 = 0$ and $\mu_2 \neq 0$ respectively, it was found that the results of $\langle \Gamma \rangle$ and μ_2 depend on the delay time range being fit, as shown in Table 3. As the delay time range is increased, the uncertainties in parameters decrease. However the values of $\langle \Gamma \rangle$ still do not stabilize and the value of μ_2 not only has a strong dependence on the delay time range being fit but also is negative. It's a contradiction with its definition. For the five independent DLS data measured at a scattering angle of 90° , the values of μ_2 also show a strong dependence on the DLS measurements and the width of the apparent hydrodynamic radius cannot be determined at this scattering angle.

Figure 2a shows the normalized time auto-correlation function of the scattered light intensity $g^{(2)}(\tau)$ for Latex-1 at a scattering angle of 90° . Equation 4 was fit to the data with $\mu_2 = 0$. The residuals vary randomly as the delay time is changed. Figure 2b shows the same data with a fit of Eq. 4 in which $\mu_2 \neq 0$. Again, the residuals are also random. The value of the apparent hydrodynamic

Delay time (s)	$\langle\Gamma\rangle_{first} (s^{-1})$	χ^2	$\langle\Gamma\rangle_{two} (s^{-1})$	$\mu_2 (s^{-2})$	χ^2
2×10^{-7} to 1.92×10^{-4}	2310 ± 14	0.46	2252 ± 47	-705056 ± 533695	0.44
2×10^{-7} to 3.072×10^{-4}	2314 ± 10	0.45	2290 ± 30	-210755 ± 241864	0.45
2×10^{-7} to 4.608×10^{-4}	2315 ± 9	0.43	2301 ± 22	-91973 ± 135873	0.43
2×10^{-7} to 7.168×10^{-4}	2316 ± 8	0.42	2301 ± 18	-87254 ± 90911	0.41
2×10^{-7} to 0.00113	2317 ± 8	0.45	2293 ± 16	-138033 ± 76731	0.42

Table 3: The fit results obtained using Eq. 4 with $\mu_2 = 0$ and $\mu_2 \neq 0$ respectively for Latex-1 at different delay time ranges, a scattering angle of 90° and a temperature of 298.45 K.

radius is 37.4 ± 0.1 nm using the first cumulant method and 37.5 ± 0.3 nm using the first two cumulant method. The value of the apparent hydrodynamic radius obtained from the DLS technique for Latex-1 at a scattering angle of 90° is still not equal to the mean radius 33.5 nm provided by the supplier. For the other polystyrene latex sample, the situation is the same: the width of the apparent hydrodynamic radius cannot be determined using this DLS technique and the value of the apparent hydrodynamic radius is larger than that provided by the supplier.

4.2 PNIPAM samples

Equation 4 was also used to obtain decay rates for PNIPAM samples with $\mu_2 = 0$ and $\mu_2 \neq 0$ respectively. Figure 3a shows the results of fitting Eq. 4 to the PNIPAM-1 data with $\mu_2 = 0$ over the delay time range 2×10^{-7} to 0.06548 s measured at a scattering angle of 30° and a temperature of 302.38K. The residuals show systematic variations with the delay time. Figure 3b shows the same data with a fit of Eq. 4 in which $\mu_2 \neq 0$. The residuals also show systematic variations with the delay time. Fit values obtained using the both procedures for the five independent data sets are listed in Table 4 at a scattering angle of 30° and a temperature of 302.38K. The results of μ_2 show a strong dependence on the DLS measurements and the width of the apparent hydrodynamic radius cannot be determined. Using the SLS technique, the relative width of the static radius can be measured accurately and is 0.085. The value of the apparent hydrodynamic radius is $323. \pm 2.$ nm using the first cumulant method and $319. \pm 2.$ nm using the first two cumulant method. The values are much larger than the value 254.3 ± 0.1 nm obtained from the SLS technique [7]. For the other PNIPAM samples investigated, the situation is the same: the distributions that can be measured accurately using the SLS technique cannot be determined by the cumulants method and the value of the hydrodynamic radius obtained using the cumulants is larger than that obtained from the SLS technique.

	$\langle \Gamma \rangle_{first} (s^{-1})$	χ^2	$\langle \Gamma \rangle_{two} (s^{-1})$	$\mu_2 (s^{-2})$	χ^2
1	39.65 ± 0.07	0.27	39.8 ± 0.1	17 ± 14	0.26
2	39.39 ± 0.07	0.67	40.1 ± 0.1	94 ± 15	0.35
3	39.77 ± 0.07	0.46	40.0 ± 0.1	35 ± 14	0.41
4	39.62 ± 0.07	0.36	39.8 ± 0.1	17 ± 14	0.35
5	39.22 ± 0.07	1.09	40.2 ± 0.1	127 ± 16	0.50

Table 4: The fit results obtained using Eq. 4 with $\mu_2 = 0$ and $\mu_2 \neq 0$ respectively for the five independent DLS data of PNIPAM-1 at a scattering angle of 30° and a temperature of 302.38K.

5 RESULTS AND DISCUSSION

Because the expected values of the DLS data calculated based on the commercial and static particle size information are consistent with the experimental data [7, 8], the DLS simulated data were used to explore the effects of particle size distribution on the deviation between the exponentiality and $g^{(2)}(\tau)$ and the initial slope of the logarithm of $g^{(2)}(\tau)$ at a scattering angle of 30° . The method that produces the DLS simulated data has been detailed before [7]. In this work, the number distribution of particle sizes is still chosen as a Gaussian distribution

$$G(R_s; \langle R_s \rangle, \sigma) = \frac{1}{\sigma\sqrt{2\pi}} \exp\left(-\frac{1}{2} \left(\frac{R_s - \langle R_s \rangle}{\sigma}\right)^2\right), \quad (8)$$

where $\langle R_s \rangle$ is the mean static radius and σ is the standard deviation related to the mean static radius.

The simulated data were produced using the information: the mean static radius $\langle R_s \rangle$, standard deviation σ , temperature T , viscosity of the solvent η_0 , scattering angle θ , wavelength of laser light λ , refractive index of the water n_s and constant $a = R_h/R_s$ were set to 50 nm, 10 nm, 300.49K, 0.8479 mPa·S, 30° , 632.8 nm, 1.332 and 1.1, respectively. When the data of $(g^{(2)}(\tau) - 1)/\beta$ were obtained, the 1% statistical noises were added and the random errors were set 3%. Five simulated data were produced respectively. The fit results for one of the DLS simulated data at different delay time ranges using Eq. 4 with $\mu_2 = 0$ and $\mu_2 \neq 0$ respectively are listed in Table 5.

The fit results at different delay time ranges shown in Table 5 are the same situation as the results of Latex-1 at a scattering angle of 30° . When Eq. 4 was used to fit the data of the simulated data produced based on the mean static radius 50 nm and standard deviation 10 nm, it was found that the results of $\langle \Gamma \rangle$ and μ_2 depend on the delay time range being fit. If a small delay time range is chosen, the parameters are not well-determined. As the delay time range is increased, the uncertainties in parameters decrease and $\langle \Gamma \rangle$ and μ_2 stabilize. The fit results for $g^{(2)}(\tau)$ are shown in Fig. 4. For both the fit results, the residuals are random as the delay time is changed. From Eq. 6, the relative width of the apparent hydrodynamic radius is about 0.16. It is different from the

Delay time range (s)	$\langle\Gamma\rangle_{first} (s^{-1})$	χ^2	$\langle\Gamma\rangle_{two} (s^{-1})$	$\mu_2 (s^{-2})$	χ^2
2×10^{-7} to 0.00402	186.78 ± 0.09	1.09	188.9 ± 0.5	1237 ± 265	0.98
2×10^{-7} to 0.00602	186.67 ± 0.08	1.11	188.3 ± 0.3	843 ± 158	0.97
2×10^{-7} to 0.00802	186.60 ± 0.07	1.14	188.1 ± 0.2	768 ± 116	0.93
2×10^{-7} to 0.01002	186.18 ± 0.07	1.85	188.2 ± 0.2	786 ± 56	0.92
2×10^{-7} to 0.01202	185.67 ± 0.06	3.16	188.3 ± 0.1	842 ± 39	0.92
2×10^{-7} to 0.01402	184.42 ± 0.05	7.90	188.4 ± 0.1	905 ± 24	0.92
2×10^{-7} to 0.01602	183.44 ± 0.04	12.51	188.4 ± 0.1	904 ± 19	0.88

Table 5: The fit results of simulated data produced based on the mean static radius 50 nm and standard deviation 10 nm at different delay time ranges using Eq. 4 with $\mu_2 = 0$ and $\mu_2 \neq 0$ respectively.

relative width of this simulated data 0.2. The fit results for the five simulated data also show that the values of mean decay constant $\langle\Gamma\rangle$ are consistent and the results of μ_2 have some differences for the different noises and errors like the values of μ_2 of Latex-1 at a scattering angle of 30° .

The fit results for other particle size distributions also have been analyzed. The simulated data were produced using the same temperature T , viscosity of the solvent η_0 , scattering angle θ , wavelength of laser light λ and refractive index of the water n_s . The constant a for the mean static radius 50 nm and standard deviations 3 nm, 5 nm, 15 nm, 20 nm and 25 nm was chosen to 1.1 and for the mean static radius 260 nm and standard deviations 16 nm, 26 nm, 52 nm, 78 nm, 104 nm and 130 nm was set to 1.2, respectively. The results fit Eq. 4 to one of the simulated data produced using the mean static radius 50 nm and standard deviation 3 nm at different delay time ranges are listed in Table 6. It was found that the values of $\langle\Gamma\rangle$ are consistent and the results of μ_2 strongly depend on the delay time range being fit. The fit values of the simulated data produced using the mean static radius 260 nm and standard deviation 130 nm stabilize as the delay time range is increased, but the relative width of apparent hydrodynamic radius obtained using Eq. 6 is only about 0.23. The fit results for $g^{(2)}(\tau)$ are shown in Fig. 5. For both the fit results, the residuals are random.

From the analysis of the simulated data, the width of apparent hydrodynamic radius cannot be determined for narrow distributions because the values of μ_2 have a strong dependence on the noises, errors or delay time range being fit and can be determined for wide particle size distributions since the values of $\langle\Gamma\rangle$ and μ_2 stabilize as the delay time range being fit is increased. However, the value of the relative width of apparent hydrodynamic radius obtained using the DLS technique has largely different from the relative width of the simulated data being fit. Because the standard method of cumulants obtains the distribution of apparent hydrodynamic radius from the deviation between the exponentiality and $g^{(2)}(\tau)$ measured at a single scattering angle, the simulated data were used to explore the nonexponentiality of $g^{(2)}(\tau)$ at a scattering angle of 30° . The logarithm of the simulated data produced without noises and errors were plotted

Delay time (s)	$\langle \Gamma \rangle_{first} (s^{-1})$	χ^2	$\langle \Gamma \rangle_{two} (s^{-1})$	$\mu_2 (s^{-2})$	χ^2
2×10^{-7} to 0.004	216.9 ± 0.1	1.12	218.6 ± 0.5	1009 ± 326	1.08
2×10^{-7} to 0.00442	216.9 ± 0.1	1.07	218.4 ± 0.5	868 ± 302	1.03
2×10^{-7} to 0.00642	216.9 ± 0.1	1.02	218.0 ± 0.4	598 ± 255	1.00
2×10^{-7} to 0.00842	217.0 ± 0.1	0.98	217.0 ± 0.2	8 ± 89	0.99
2×10^{-7} to 0.01042	216.83 ± 0.04	1.20	217.1 ± 0.2	59 ± 30	1.19
2×10^{-7} to 0.01242	216.75 ± 0.04	1.25	217.3 ± 0.1	97 ± 27	1.20
2×10^{-7} to 0.01442	216.73 ± 0.04	1.23	217.3 ± 0.1	106 ± 25	1.16

Table 6: The fit results of simulated data produced based on the mean static radius 50 nm and standard deviation 3 nm at different delay time ranges using Eq. 4 with $\mu_2 = 0$ and $\mu_2 \neq 0$ respectively.

as a function of the delay time. All results for the standard deviations 3 nm, 10 nm, 20 nm, 25 nm and mean static radius 50 nm are shown in Fig. 6a and the standard deviations 16 nm, 52 nm, 104 nm, 130 nm and mean static radius 260 nm are shown in Fig. 6b, respectively. Figure 6 shows the effects of the standard deviation are small on the nonexponentiality of $g^{(2)}(\tau)$ and large on the initial slope of the logarithm of $g^{(2)}(\tau)$ $\langle \Gamma \rangle$ at a scattering angle of 30° .

Because the apparent hydrodynamic radius is related to $\langle \Gamma \rangle$, the effects of the particle size distribution on the apparent hydrodynamic radius were thus explored. The values of the apparent hydrodynamic radius obtained using Eqs. 4 and 5 with $\mu_2 = 0$ and $\mu_2 \neq 0$, and Eq. 7 respectively for the simulated data produced using the mean static radius 50 nm and different standard deviations are shown in Table 7. From the relationship $a = R_h/R_s = 1.1$, the mean hydrodynamic radius $\langle R_h \rangle$ is 55 nm. The relative deviations $(R_{h,app1} - \langle R_h \rangle) / \langle R_h \rangle$ as a function of the standard deviation are also listed in Table 7.

$\sigma / \langle R_s \rangle$	$R_{h,app1} (nm)$	$R_{h,app2} (nm)$	$R_{cal} (nm)$	$\frac{R_{h,app1} - \langle R_h \rangle}{\langle R_h \rangle}$
0.06	56.2 ± 0.2	56.2 ± 0.5	56.1	0.02
0.1	57.9 ± 0.2	57.5 ± 0.2	57.9	0.05
0.2	65.3 ± 0.1	64.6 ± 0.1	65.4	0.19
0.3	75.5 ± 0.5	73.8 ± 0.4	75.5	0.37
0.4	87.1 ± 0.6	84.4 ± 0.5	86.8	0.58
0.5	99.8 ± 0.8	96.3 ± 0.8	98.7	0.81
0.6	$112. \pm 1.$	108.1 ± 0.9	110.9	1.04
0.7	125.0 ± 0.7	$120. \pm 1.$	123.2	1.27

Table 7: Values of $R_{h,app}$ for the simulated data produced using the mean static radius 50 nm and different standard deviations, and relative deviations $(R_{h,app1} - \langle R_h \rangle) / \langle R_h \rangle$.

The results in Table 7 show that the value of the apparent hydrodynamic ra-

dius is greatly influenced by the particle size distribution. The part of apparent hydrodynamic radius represents the effects of particle size distributions. The wider the particle size distribution, the larger the value of the apparent hydrodynamic radius. The consistency between the value calculated from Eq. 7 and the result obtained using the first cumulant also shows the deviation between the exponentiality and $g^{(2)}(\tau)$ at a scattering angle of 30° is small even for very wide distribution like the relative width distribution 50%. The difference between the results obtained using the first and first two cumulants is influenced by the particle size distribution. For narrow distributions, they are almost equal. For a wide distribution like 50%, the difference is less than 4%. The relative width of apparent hydrodynamic radius obtained from the deviation between the exponentiality and $g^{(2)}(\tau)$ is about 24% for the simulated data produced using the relative width of hydrodynamic radius 50%. This difference is caused by the method of cumulants. The average decay rate of $g^{(2)}(\tau)$ is determined by the particle size distribution and the relationship between the static and hydrodynamic radii together and the method of cumulants measures the width of apparent hydrodynamic radius from the nonexponentiality of $g^{(2)}(\tau)$ related to the exponentiality of the average decay rate at a single scattering angle.

6 CONCLUSION

The effects of the particle size distribution on the nonexponentiality of $g^{(2)}(\tau)$ are small and very large on the initial slope of the logarithm of $g^{(2)}(\tau)$ at a scattering angle of 30° . The values of the apparent hydrodynamic radius are also greatly influenced by the particle size distribution. The wider the particle size distribution, the larger the value of the apparent hydrodynamic radius. The questions that the standard DLS techniques are not suited to the accurate determination for the poly-dispersities (standard deviation/mean size) less than 10% and the distribution of apparent hydrodynamic radius is different from the distribution of hydrodynamic radius of particles are caused by the method of cumulants. The average decay rate (the initial slope of the logarithm) of $g^{(2)}(\tau)$ is determined by the particle size distribution and the relationship between the static and hydrodynamic radii together and the method of cumulants detects the width of apparent hydrodynamic radius from the nonexponentiality of $g^{(2)}(\tau)$ related to the exponentiality of the average decay rate at a single scattering angle. The situations that the standard method of cumulants are used at other scattering angles will be studied further.

Fig. 1. The experimental data and fit results of $g^{(2)}(\tau)$ for Latex-1 at a scattering angle of 30° and a temperature of 298.45 K. The circles show the experimental data, the line represents the fit results obtained using Eq. 4 and the diamonds show the residuals $(y_i - y_{fit})/\sigma_i$. The results for $\mu_2 = 0$ and $\mu_2 \neq 0$ are shown in a and b respectively.

Fig. 2. The experimental data and fit results of $g^{(2)}(\tau)$ for Latex-1 at a scattering angle of 90° and a temperature of 298.45 K. The circles show the experimental data, the line represents the fit results obtained using Eq. 4 and

the diamonds show the residuals $(y_i - y_{fit})/\sigma_i$. The results for $\mu_2 = 0$ and $\mu_2 \neq 0$ are shown in a and b respectively.

Fig. 3. The experimental data and fit results of $g^{(2)}(\tau)$ for PNIPAM-1 at a scattering angle of 30° and a temperature of 302.38K. The circles show the experimental data, the line represents the fit results obtained using Eq. 4 and the diamonds show the residuals $(y_i - y_{fit})/\sigma_i$. The results for $\mu_2 = 0$ and $\mu_2 \neq 0$ are shown in a and b respectively.

Fig. 4. The fit results of $g^{(2)}(\tau)$ for the simulated data produced based on the mean static radius 50 nm and standard deviations 10 nm at a scattering angle of 30° . The circles show the simulated data, the line represents the fit results obtained using Eq. 4 and the diamonds show the residuals $(y_i - y_{fit})/\sigma_i$. The results for $\mu_2 = 0$ and $\mu_2 \neq 0$ are shown in a and b respectively.

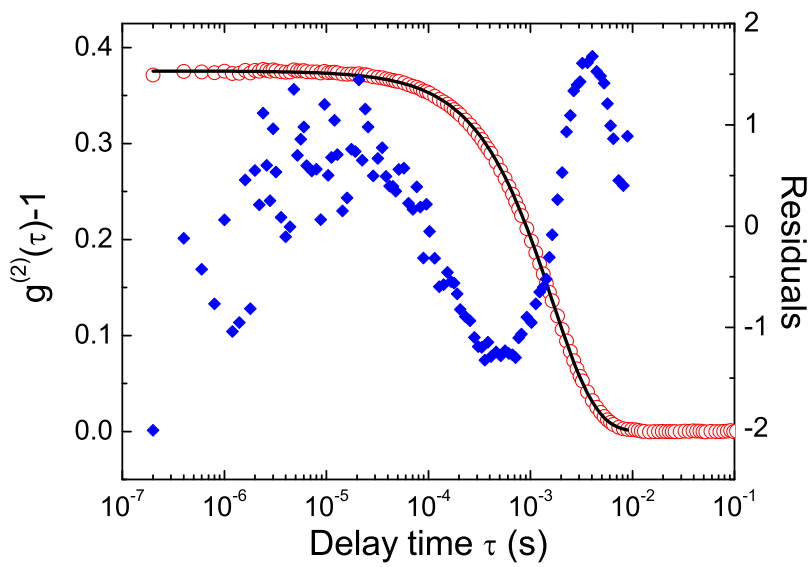
Fig. 5. The fit results of $g^{(2)}(\tau)$ for the simulated data produced with the mean static radius 260 nm and standard deviations 130 nm at a scattering angle of 30° . The circles show the simulated data, the line represents the fit results obtained using Eq. 4 and the diamonds show the residuals $(y_i - y_{fit})/\sigma_i$. The results for $\mu_2 = 0$ and $\mu_2 \neq 0$ are shown in a and b respectively.

Fig. 6. The differences between the lines and plots of $\ln((g^{(2)}(\tau) - 1)/\beta)$ as a function of the delay time. The symbols show the simulated data and the lines show the linear fitting to the simulated data respectively. The results for the simulated data produced using the mean static radius 50 nm and 260 nm are shown in a and b respectively.

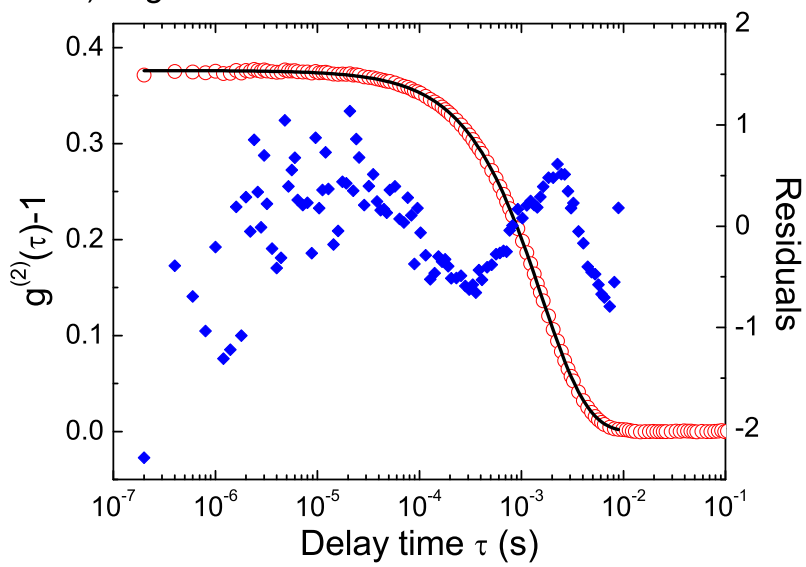
References

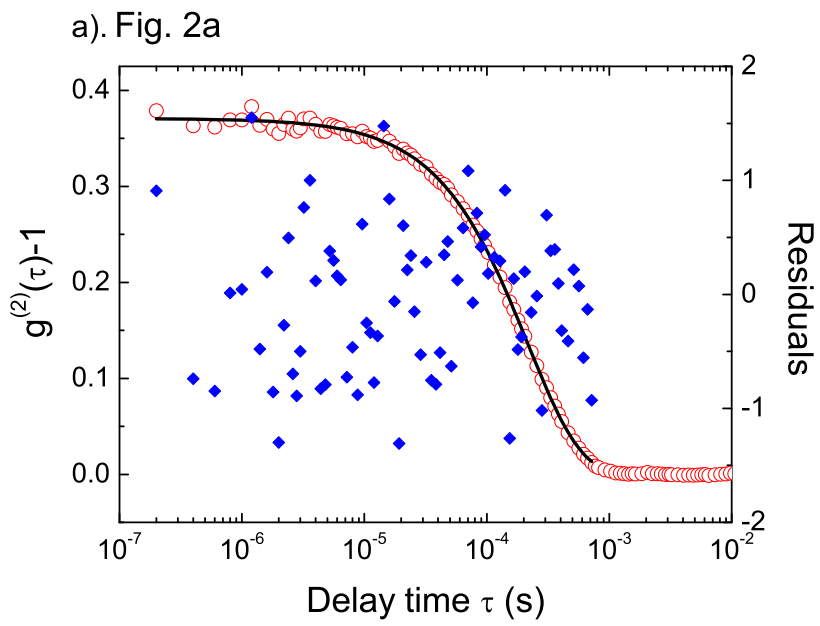
- [1] D. E. Koppel, J. Chem. Phys. **57**, 4814(1972).
- [2] C. B. Bargeron, J. Chem. Phys. **61**, 2134(1974).
- [3] J. C. Brown, P. N. Pusey and R. Dietz, J. Chem. Phys. **62**, 1136(1975).
- [4] B. J. Berne and R. Pecora, *Dynamic Light Scattering* (Robert E. Krieger Publishing Company, Malabar, Florida, 1990).
- [5] G. Bryant, S. Martin, A. Budi and W. van Megen, Langmuir **19**, 616(2003).
- [6] P. N. Pusey and W. van Megen, J. Chem. Phys. **80**, 3513(1984).
- [7] Y. Sun Unpublished (First)
- [8] Y. Sun Unpublished (Second).
- [9] The ALV Manual of the Version for ALV-5000/E for Windows, ALV-GmbH, Germany, 1998.

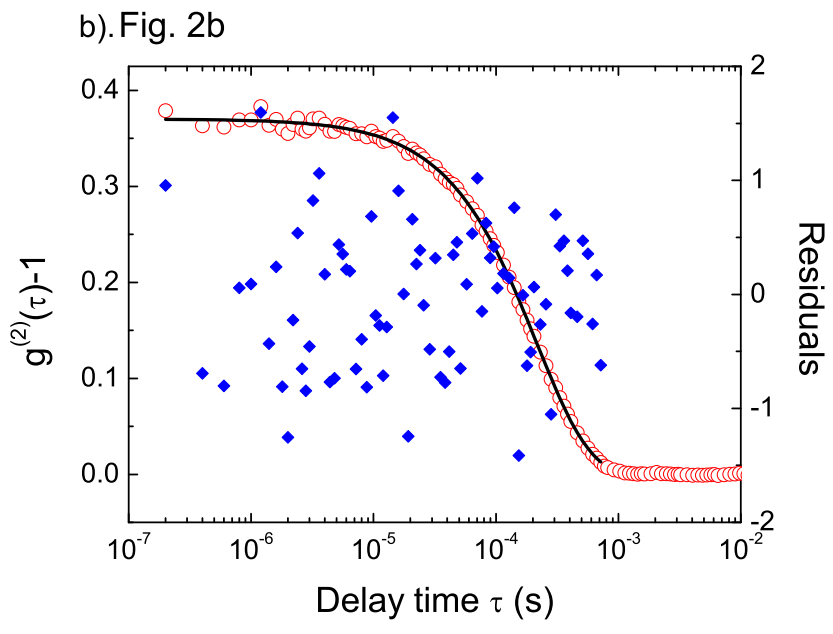
a). Fig. 1a

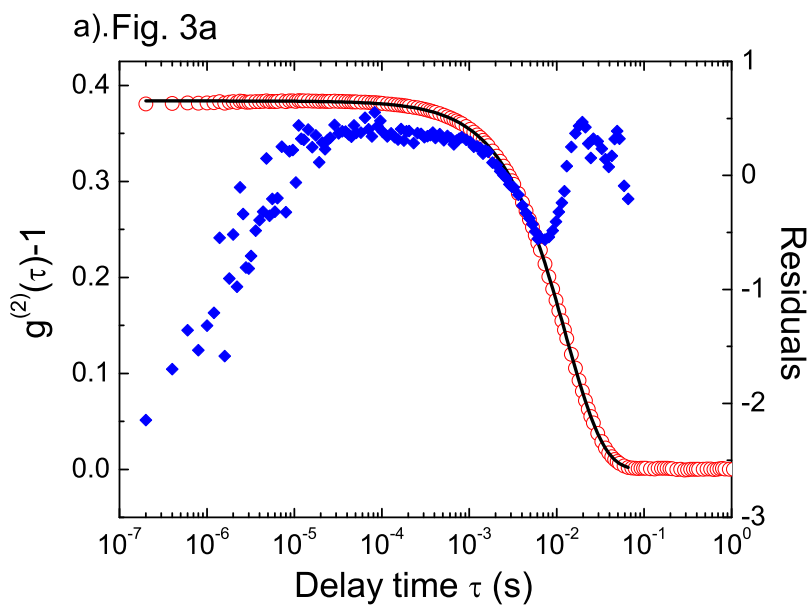


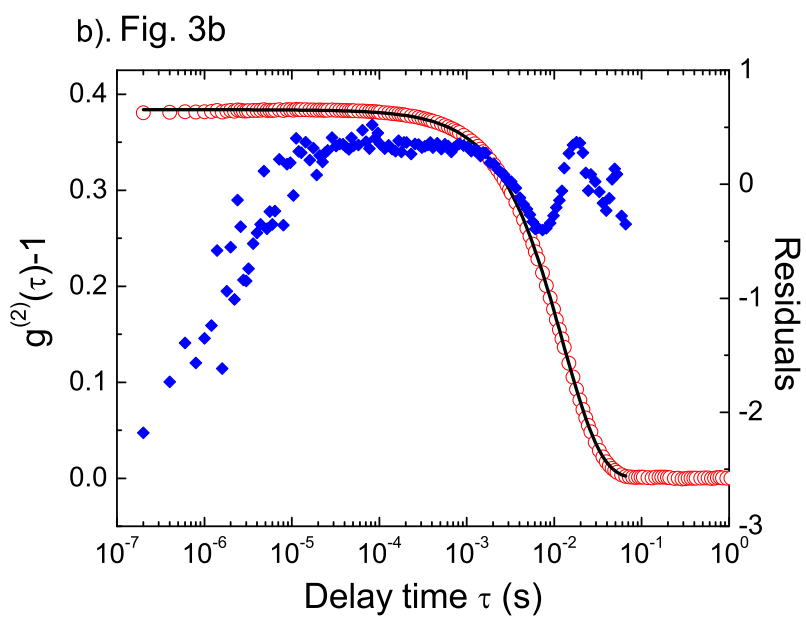
b). Fig. 1b

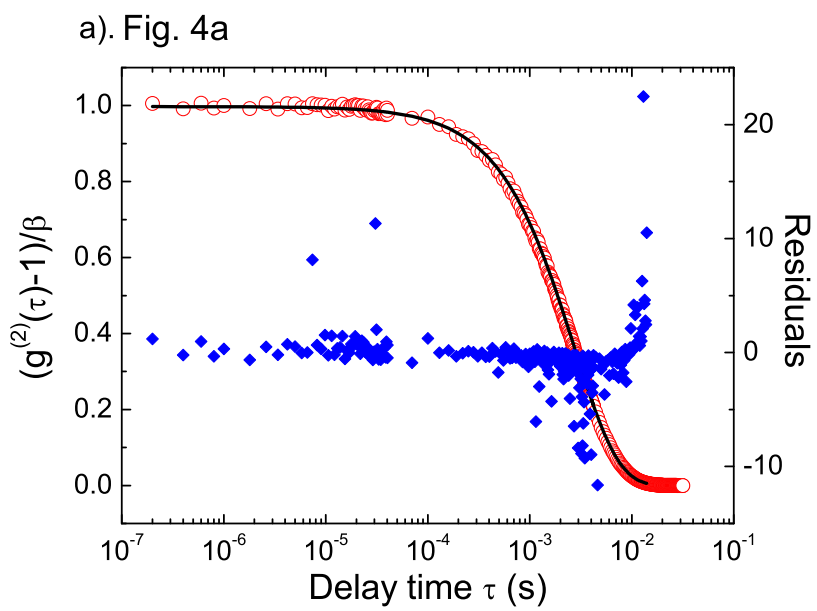


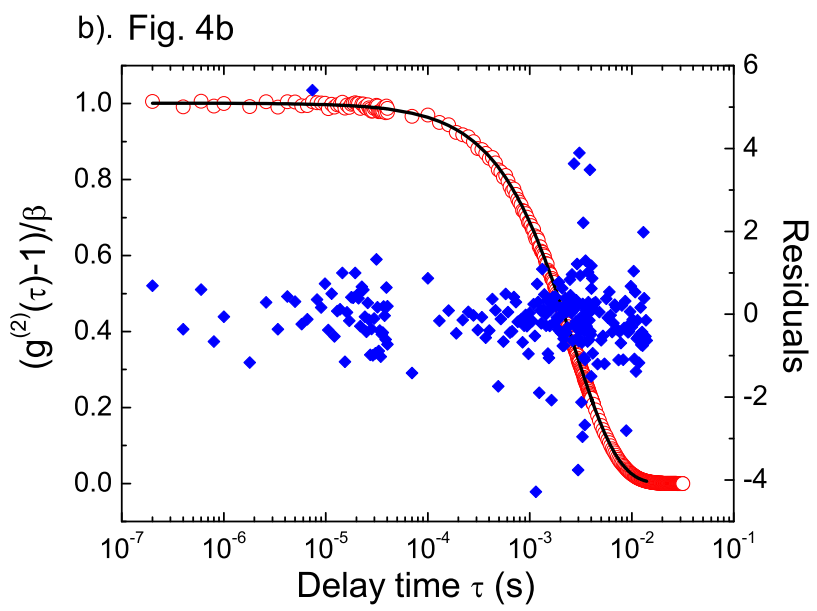




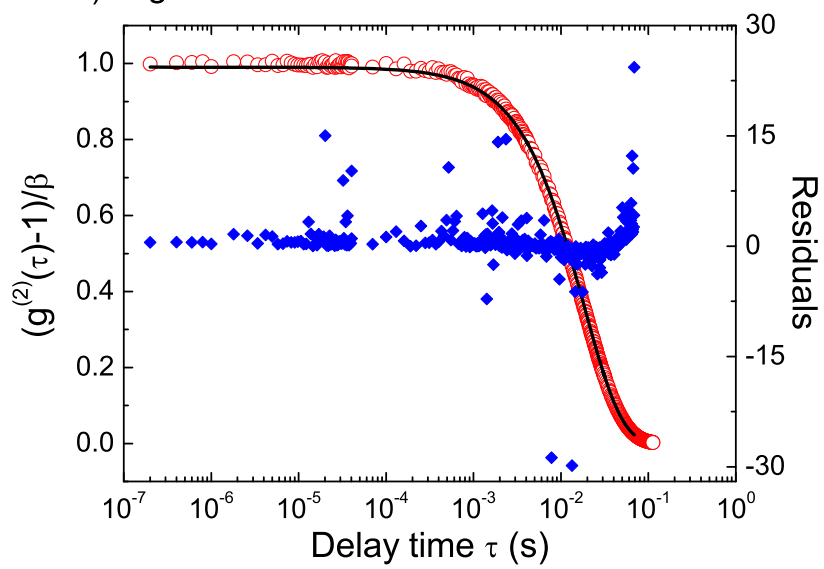


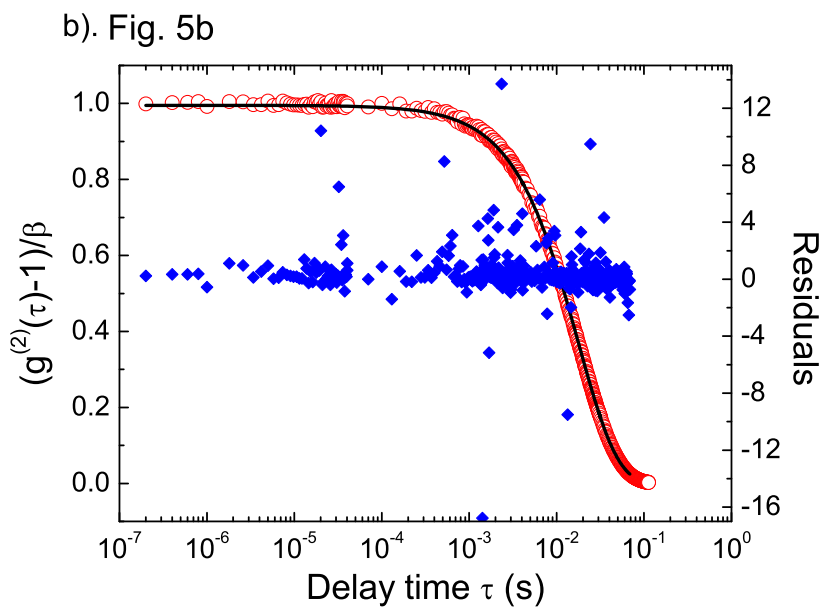




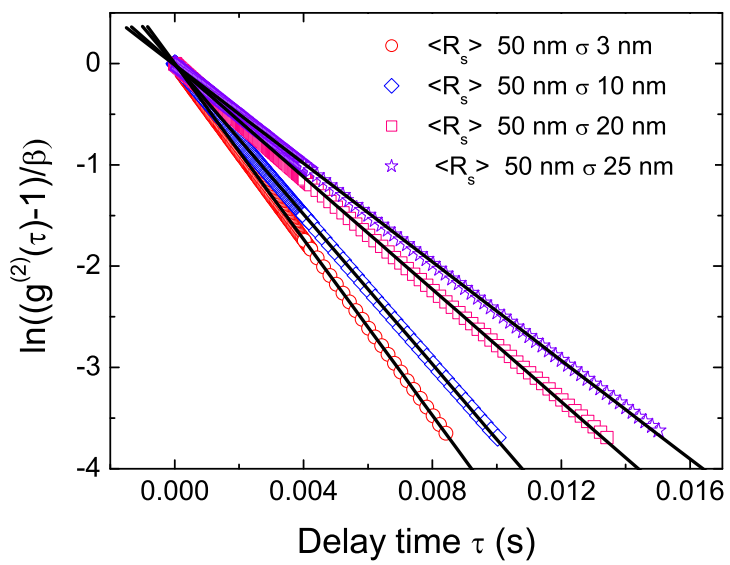


a). Fig. 5a





a). Fig. 6a



b). Fig. 6b

